

ARTICLE OPEN



Non-synchronous bulk photovoltaic effect in two-dimensional interlayer-sliding ferroelectrics

Rui-Chun Xiao¹, Yang Gao^{2✉}, Hua Jiang³, Wei Gan¹, Changjin Zhang^{1,4} and Hui Li^{1✉}

Spontaneous polarization and bulk photovoltaic effect (BPVE) are two concomitant physical properties in ferroelectric materials. The flipping of ferroelectric order usually accompanies the switching of BPVE in all directions because both of them are reversed under the inversion symmetry. In this study, we report the non-synchronous BPVE in two-dimensional (2D) interlayer-sliding ferroelectric materials featuring unswitchable in-plane BPVE (light-induced photocurrent in the xy plane) and switchable out-of-plane BPVE (light-induced polarization along the z -direction). Symmetry analysis within the abstract bilayer crystal model and first-principles calculations validate these BPVE properties. It is because the positive and negative ferroelectric states caused by interlayer sliding are related by mirror symmetry which cannot flip all the BPVE tensor elements. This finding extends the understanding of the relationship between ferroelectricity and BPVE. On one hand, the switchable out-of-plane BPVE can be used to design switchable photoelectric devices. On the other hand, the in-plane BPVE is robust against the ferroelectric flipping, and the unswitchable character is beneficial to construct larger-scale photoelectric devices.

npj Computational Materials (2022)8:138; <https://doi.org/10.1038/s41524-022-00828-1>

INTRODUCTION

Ferroelectricity and bulk photovoltaic effect (BPVE)^{1,2} are two basic physical phenomena that emerge in condensed matter materials due to symmetry breaking. Generally speaking, BPVE, an intrinsic optical rectification phenomenon, appears in materials without inversion symmetry which can convert light to electricity as solar cells, hence it is naturally fulfilled the symmetry requirement in ferroelectric materials. As a result, the ferroelectric materials with switchable electronic polarization are one of the most studied BPVE materials^{1–3}, and the corresponding energy conversion efficiency can exceed the Shockley-Queisser limit^{3–5}.

It is known to us that the BPVE usually switches with the ferroelectric order. Under the inversion operation, both ferroelectric order and BPVE in all directions switch signs, i.e., BPVE switches synchronously with the ferroelectric order. Therefore, the ferroelectric polarization is often taken as a handle to manipulate the direction of BPVE photocurrent in, e.g., perovskite oxides BiFeO₃^{6–8}, Pt/BiFeO₃/SrRuO₃⁹, 2D (two-dimensional) CuInP₂Se₆¹⁰, charge-transfer complex¹¹, SnTe monolayer¹², MX [M = (Ge, Sn) and X = (Se, S)]¹³ etc. However, from the aspect of symmetry, the ferroelectric polarization is a polar vector, while the BPVE coefficients form a rank-three tensor. They are hence subject to distinct symmetry transformation rules, and should not always synchronize. There should exist components of the BPVE tensor that do not switch with the ferroelectric order, which was visioned¹⁴, but has not been comprehensively studied before. For example, a mirror reflection perpendicular to the polarization will reverse the polarization just as the inversion operation does, while it cannot flip all the components of the BPVE. Thus, a precise understanding of the relationship between the ferroelectric order and the BPVE is of tremendous significance in both fundamental research and the design of photoelectric devices.

In this work, we think the exceptional case that non-synchronous BPVE with ferroelectric order can be found in 2D

interlayer-sliding ferroelectric materials¹⁵. As demonstrated in recent experiments, the out-of-plane ferroelectricity can be achieved in bilayer WTe₂^{16–19}, BN^{20,21}, InSe^{22,23}, MoS₂^{24,25}, etc. by interlayer sliding, which effectively extends the family of 2D ferroelectric materials^{26–29}. This ferroelectric flip mechanism may lead to the BPVE property beyond the switchable scenario.

Focusing on the four most common stacking cases of 2D bilayers with interlayer sliding, we use an abstract bilayer crystal model to locate the available configurations and symmetries with nontrivial ferroelectric order. We find two cases (Case 1b and Case 2a) can have the possibility to achieve the interlayer-sliding ferroelectricity, moreover the opposite ferroelectric states in the two cases are all related by the mirror operator. Coincidentally, the interlayer-sliding ferroelectric materials found in the experiments are attributed to these two cases. Using bilayer MoS₂ and WTe₂ as representative examples, we performed first-principles calculations and found that the in-plane BPVE does not change the sign with ferroelectric order, which is different from conventional ferroelectrics. In contrast to in-plane BPVE, out-of-plane BPVE switches with the reverse of the ferroelectric order. This non-synchronous character will lead to distinct photovoltaic phenomena in experiments.

RESULTS

Polarization flipping via interlayer sliding

Now we introduce the mechanism of the polarization flipping via interlayer sliding. Figure 1a shows the out-of-plane polarization P_z in bilayer vdW (van der Waals) material without inversion nor horizontal mirror symmetry. Because the in-plane polarization is usually annihilated by in-plane rotational symmetry in real materials, the $+P_z$ and $-P_z$ polarization are denoted as $+P$ and $-P$ for short. The out-of-plane polarization can be flipped in two different ways: (i) intralayer movement, i.e., atomic relative

¹Institute of Physical Science and Information Technology and Information Materials and Intelligent Sensing Laboratory of Anhui Province, Anhui University, Hefei 230601, China.

²Department of Physics, University of Science and Technology of China, Hefei 230026, China. ³School of Physical Science and Technology, Soochow University, Suzhou 215006, China. ⁴High Magnetic Field Laboratory, Chinese Academy of Sciences, Hefei 230031, China. ✉email: ygao87@ustc.edu.cn; huili@ahu.edu.cn

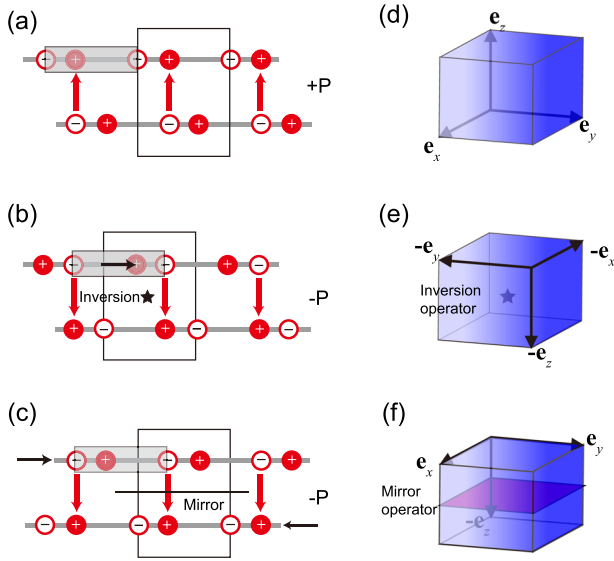


Fig. 1 Polarization flipping in a 2D vdW bilayer material via intralayer movement or interlayer sliding, and related symmetries. **a** A 2D system with positive out-of-plane polarization $+P$. **b** The polarization is reversed to $-P$ by atom displacements in each monolayer, and the black arrow means the movement of the cations relative to the anions. **c** The polarization is reversed by interlayer sliding and the black arrows mean the interlayer sliding direction. **d** Three basis vectors and their transformations under **e** inversion symmetry **f** horizontal mirror symmetry. The black rectangles denote the bilayer unit cells in (a)–(c), and the gray rectangles denote the monolayer unit cells.

displacements in each monolayer [Fig. 1b], and (ii) interlayer sliding¹⁵ where the crystal structure of each monolayer is invariant [Fig. 1c]. Although polarization flipping can be achieved in both situations, the underlying symmetries of the switch of ferroelectric states are different. For situation (i), the $+P$ and $-P$ ferroelectric states are correlated by the inversion operator, as indicated in unit cells in Fig. 1a, b. While for situation (ii), the $+P$ and $-P$ ferroelectric states are correlated by the mirror symmetry \hat{M}_{xy} , as seen in unit cells in Fig. 1a, c (detailed analyses are presented in the Symmetry analysis section for real materials). The interlayer sliding mechanism is feasible experimentally and has been observed in bilayer vdW materials^{16–25} as stated above, which further extends the family of 2D ferroelectric materials^{26–29} effectively. Figure 1d–f shows the basis vector transformation under the inversion symmetry and mirror symmetry. The BPVEs in these interlayer-sliding ferroelectric materials do not always change synchronously with the ferroelectric order.

Symmetry analysis

Next, we analyze how to design the bilayer vdW materials with the out-of-plane polarization via interlayer sliding in Fig. 1a, and analyze how positive and negative polarizations are related by symmetry operator. Most of the discovered monolayer materials are non-polar and non-ferroelectric (such as BN, transition-metal dichalcogenides, metal trihalide, post-transition-metal chalcogenides), and their monolayer crystal structures belong to the following two different cases, as shown in Supplementary Figs. 1, 2 in the Supplementary Information^{30,31}:

1. Monolayer has the inversion symmetry \hat{I} , but has no horizontal mirror symmetry \hat{M}_{xy} , such as monolayer 1T-PtS₂, 1T-WTe₂, BiI₃, etc.;
2. Monolayer has no inversion symmetry \hat{I} but has horizontal

mirror symmetry \hat{M}_{xy} , such as monolayer BN, 1H-MoS₂, 1H-WSe₂, GaSe, InSe, etc.

Besides, the bilayer can be further divided into two subcases according to the stacking manner of two layers:

- (a) A/A stacking, i.e., two adjacent layers are identical where the A represents the crystal structure of the monolayer.
- (b) A/B stacking, i.e., two adjacent layers are relatively rotated by 180° with $B = \hat{C}_{2z}A$ (A and B mean the crystal types).

The above considerations can form four cases for 2D bilayer materials with interlayer sliding, and we can analyze their symmetries with an abstract bilayer crystal model which only considers the above crystal symmetries and ignores the specific crystal structures. The complete symmetry analysis for each case is summarized in Supplementary Note 1, and the corresponding results are shown in Table 1. As can be seen, Case 1b and Case 2a host the out-of-plane polarization, and the two opposite interlayer-sliding states are correlated by \hat{M}_{xy} operator, instead of inversion \hat{I} operator. In contrast, the crystal structures in Case 1a and Case 2b possess the inversion symmetry whatever the interlayer-sliding vector, which forbids the occurrence of ferroelectricity and BPVE.

With the abstract bilayer crystal model, the interlayer-sliding ferroelectric materials are further classified into two kinds (Case 1b and Cases 2a). Such classification outlines a potential roadmap to search for more 2D ferroelectric materials, which could greatly facilitate and advance the research and application of BPVE in 2D ferroelectric materials. Table 2 summarizes several bilayer candidates for the above four cases that can be experimentally realized by either simply mechanical exfoliation or tear-and-stack methods. In particular, the out-of-plane ferroelectricity of the bilayer WTe₂^{16–19} with Case 1b and BN^{20,21}, InSe^{22,23}, bilayer-TMD^{24,25} with Case 2a have been discovered in experiments recently. The abstract bilayer model is convenient and efficient in symmetry analysis for vdW materials with interlayer sliding because it does not rely on the specific crystal structure. The symmetry of trilayer vdW materials with interlayer sliding can also be obtained using a similar method, and the results are shown in Supplementary Note 7, where the transformations of ferroelectricity and BPVE are also discussed there.

Now we analyze the characters of in-plane and out-of-plane BPVE of the interlayer-sliding ferroelectric materials in Case 1b and Case 2a under the normal incidence of light. The in-plane BPVE current density is

$$J_a = \sum_{bc} \sigma_{bc}^a E_b(\omega) E_c(-\omega), \quad (1)$$

where $a, b, c \in \{x, y\}$, E_b and E_c are electric fields of light along b and c direction, ω is the frequency of light, and σ_{bc}^a is the BPVE coefficient. In contrast to x and y directions, the photo-excited shift of the wave package along the out-of-plane direction induces a static electric polarization instead of an electric current along the z -direction because the z -direction of 2D materials is discontinuous. The out-of-plane BPVE polarization is³²

$$p_z = \sum_{bc} \sigma_{bc}^z E_b(\omega) E_c(-\omega), \quad (2)$$

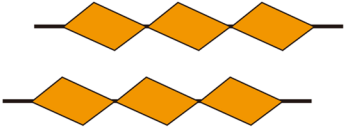
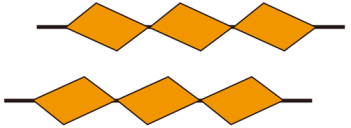
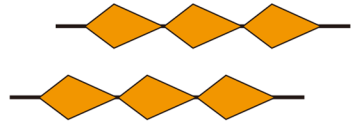
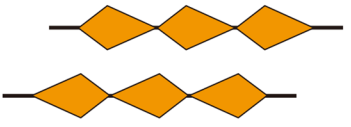
where p_z is z -component polarizability.

Similar to other nonlinear optics tensors, the BPVE tensor $[\sigma_{ab}^c]_{3 \times 3 \times 3}$ in Eq. (1) [or Eq. (2)] obeys

$$\sigma_{jk}^i = \sum_{abc} R_{ia} R_{jb} R_{kc} \sigma_{bc}^a, \quad (3)$$

where $[R_{ia}]$ is the 3×3 matrix of the symmetry operator \hat{R} . As shown in Fig. 1f, \hat{M}_{xy} will result in the reverse of the out-of-plane vector with invariant in-plane vectors, and the corresponding

Table 1. Symmetries of interlayer-sliding bilayer materials.

Stacking way Monolayer symmetry	a. A/A	b. A/B
1. $\begin{cases} \hat{I}: \checkmark \\ \widehat{M}_{xy}: \times \end{cases}$	 Case 1a: $\begin{cases} \hat{I}: \checkmark \\ \widehat{M}_{xy}: \times \end{cases}$	 Case 1b: $\begin{cases} \hat{I}: \times \\ \widehat{M}_{xy}: \times \\ \widehat{M}_{xy}S_+ = S_- \end{cases}$
2. $\begin{cases} \hat{I}: \times \\ \widehat{M}_{xy}: \checkmark \end{cases}$	 Case 2a: $\begin{cases} \hat{I}: \times \\ \widehat{M}_{xy}: \times \\ \widehat{M}_{xy}S_+ = S_- \end{cases}$	 Case 2b: $\begin{cases} \hat{I}: \checkmark \\ \widehat{M}_{xy}: \times \end{cases}$

(1) The crystal structures here are abstract bilayers, and the orange quadrilateral indicates the abstract unit cell of monolayer; (2) S_+ and S_- represent the bilayer with opposite sliding vectors.

Table 2. Candidate bilayer materials and corresponding symmetries of bulk parents.

	Candidate materials	Symmetry of bulk parents
Case 1a	1T-MX ₂ (PtSe ₂ , PtS ₂ , TiS ₂ , SnS ₂)	P $\bar{3}$ m1 (164)
	MX ₃ (BiI ₃)	R $\bar{3}$ (148)
Case 1b	T _d /1T'-WTe ₂ , MoTe ₂ , ZrI ₂	Pmn2 ₁ (31) or P2 ₁ m (11)
Case 2a	GaSe, InSe, InS	P $\bar{6}$ m2 (187)
	3R-MX ₂ (MoS ₂ , MoSe ₂)	R3m (160)
	BN	R3m (160)
Case 2b	h-BN	P6 ₃ /mmc (194)
	2H-MX ₂ (MoS ₂), GaS	P6 ₃ /mmc (194)
	GeSe, SnSe	Pnma (62)

(1) MX₂ means the transition-metal dichalcogenides and MX₃ means the transition-metal trihalides, (2) bulk parents mean the bulk materials which stacking with the same manners, and (3) the structure data are from Materials Project⁵⁷.

operator matrix is

$$[M_{xy}] = \begin{bmatrix} 1 & 0 & 0 \\ 0 & 1 & 0 \\ 0 & 0 & -1 \end{bmatrix}. \quad (4)$$

The opposite states are connected by the mirror operator $[\widehat{M}_{xy}(+P) = -P]$ in interlayer-sliding ferroelectric materials. Therefore, the in-plane BPVE coefficient is invariant with the change of

ferroelectric orders, i.e., $\sigma_{ab}^c(+P) = \sigma_{ab}^c(-P)$, $a, b, c \in \{x, y\}$, according to Eq. (3). This is strikingly different from the out-of-plane case where the BPVE coefficient is reversed with the switch of ferroelectric orders, as indicated by $\sigma_{bc}^z(+P) = -\sigma_{bc}^z(-P)$ ($b, c \in \{x, y\}$). The calculated BPVE characters in Fig. 1a, c by a 1D effective model are also consistent with our symmetry analysis (see Supplementary Note 2).

In contrast, for the ferroelectric states correlated by inversion symmetry $\hat{I}(+P) = -P$, the inversion operator \hat{I} will lead to the reverse of all the vectors (Fig. 1d), i.e., $\sigma_{bc}^a(+P) = -\sigma_{bc}^a(-P)$ ($a, b, c \in \{x, y, z\}$) according to Eq. (3). It is the reason why the BPVE coefficients reverse with ferroelectric orders in the conventional ferroelectric materials.

The in-plane BPVE coefficients can be calculated by the standard second-order Kubo formalism theory^{33,34}, and the out-of-plane BPVE coefficients can be obtained by a modified second-order Kubo formalism theory³² that was proposed recently. BPVE coefficients are calculated by the Wannier function (see Method for details)³⁵⁻³⁷. Recently, theory works indicate that^{38,39} BPVE coefficients are highly related to the geometry theory of electron band. In the following part, we choose a representative material for each case: bilayer MoS₂^{24,25} (Case 2a) and bilayer WTe₂¹⁶⁻¹⁹ (Case 1b) to perform the numerical first-principles calculations (see Methods section for calculation details).

First-principles calculation results

Bilayer MoS₂. Bilayer MoS₂ (Case 2a) that is consisted of two identical non-ferroelectric monolayers shows out-of-plane ferroelectricity¹⁵, which has been confirmed in experiments recently^{24,25}. Noting that conventional bilayer MoS₂ is stacked in A/B form (Case

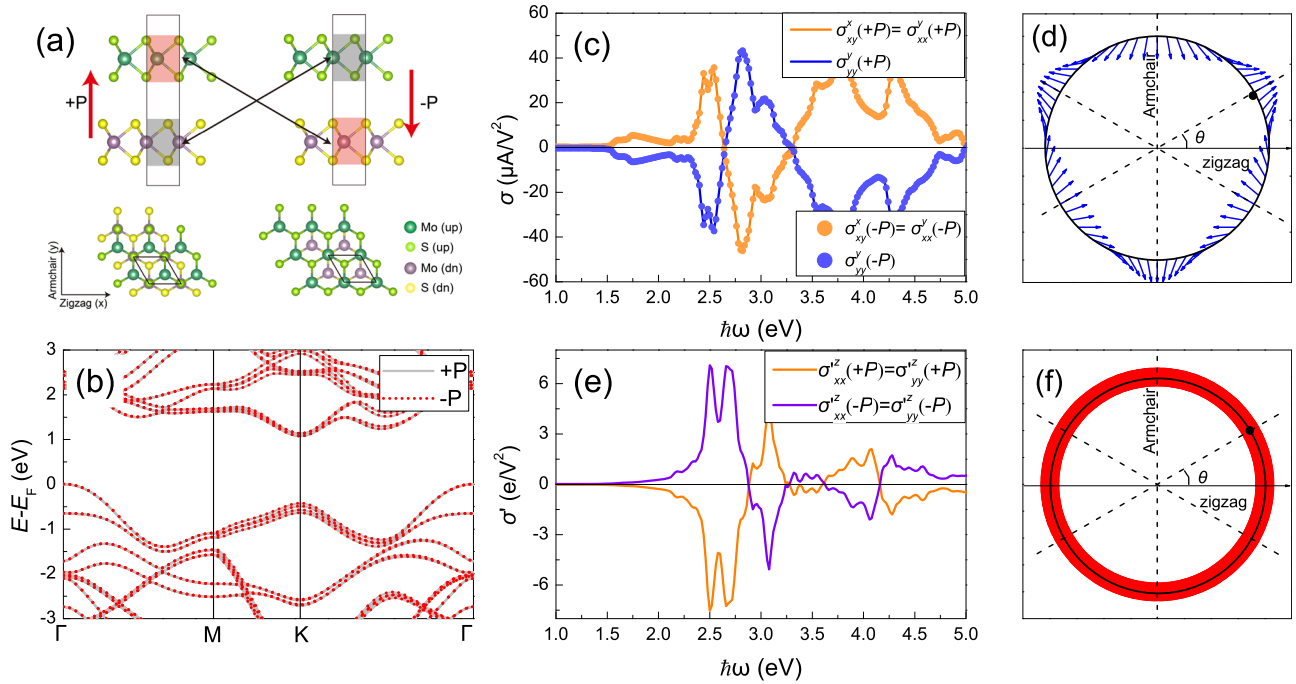


Fig. 2 Calculated results of ferroelectric bilayer MoS₂. **a** Crystal structures of ferroelectric states (upper panel: side view, lower panel: top view). The arrows denote the transformation of the +P and -P states by interlayer \hat{M}_{xy} symmetry. The definitions of +P and -P states are adopted from ref. ²⁴. **b** Band structure of +P and -P states. **c** In-plane and **e** out-of-plane BPVE coefficients. **d** In-plane BPVE photocurrent and **f** out-of-plane BPVE polarization (in arbitrary unit) with the direction of normal-incidence polarization of light in the +P states. θ in **d** and **f** is the azimuthal angle of the polarization of light relative to the x axis, and the dash lines mean the vertical mirror planes.

2b) with inversion symmetry, which is different from the crystal structure discussed here. As shown in Fig. 2a, the out-of-plane ferroelectricity is reversed by the in-plane interlayer motion along the armchair direction. The monolayer possesses the \hat{D}_{3h} symmetry. However, the interlayer-sliding bilayer breaks the \hat{M}_{xy} and in-plane \hat{C}_2 rotation symmetries, which results in the bilayer MoS₂ only having C_{3v} symmetry ($D_{3h} = C_{3v} + \hat{M}_{xy}C_{3v}$). Therefore, +P and -P states only have out-of-plane polarization. Moreover, the two ferroelectric states are connected by the \hat{M}_{xy} symmetry^{24,25}, which is consistent with the above symmetry analysis. The calculated band structures of the +P and -P states are shown in Fig. 2b, which are invariant with the ferroelectric orders.

As shown in Fig. 2c, the calculated in-plane BPVE coefficients with +P and -P states are equal. The in-plane BPVE is invariant with the change of the ferroelectric order as predicted. In addition, $\sigma_{xy}^x = \sigma_{yx}^x = -\sigma_{yy}^y$, and $\sigma_{xx}^x = \sigma_{yy}^y = \sigma_{xy}^y = 0$ for each ferroelectric state due to the C_{3v} symmetry [see Supplementary Note 3]. It is noted that this unswitchable in-plane BPVE character of interlayer-sliding ferroelectric materials is different from those of conventional ferroelectric materials^{6–12,40} and antiferromagnets^{41,42} where the BPVE is switched with the ferroelectric/ferromagnetic order. The in-plane BPVE photocurrent as a function of the polarization direction of light (see Supplementary Note 4 for details) is shown in Fig. 2d. The in-plane BPVE photocurrent shows the C_{3v} symmetry, and its magnitude is independent of the direction of light.

The calculated out-of-plane BPVE coefficients are shown in Fig. 2e. For each ferroelectric state, $\sigma_{xx}^z = \sigma_{yy}^z$, and $\sigma_{xy}^z = \sigma_{yx}^z = 0$. Moreover, the out-of-plane BPVE coefficients switch with the ferroelectric order following $\sigma_{xx}^z(+P) = \sigma_{yy}^z(+P) = -\sigma_{xx}^z(-P) = -\sigma_{yy}^z(-P)$, which is consistent with our symmetry analysis. The out-of-plane BPVE is isotropic, and photo-induced polarization is independent of the polarization direction of light due to C_{3v} symmetry, as shown in Fig. 2f.

Similarly, experimentally prepared bilayer BN^{20,21}, InSe^{22,23}, GaSe, etc., possess similar interlayer-sliding ferroelectricity (Case 2a) and the same symmetry. Therefore, similar in-plane and out-of-plane BPVE features are also expected to exhibit in these materials.

Bilayer WTe₂. Bilayer WTe₂ is composed of two 180°-rotated two monolayers (Case 1b), as shown in Fig. 3a. Even though each monolayer (with $C_{2h} = \{E, \hat{I}, \hat{C}_{2x}, \hat{M}_{yz}\}$ symmetry) has the inversion \hat{I} symmetry, the bilayer breaks this symmetry. Besides, the interlayer-sliding vector along b axis further breaks \hat{M}_{xy} and in-plane \hat{C}_2 symmetry. Thereby the bilayer has the $C_{1v} = \{E, \hat{M}_{yz}\}$ symmetry ($C_{2h} = C_{1v} + \hat{M}_{xy}C_{1v}$).

Interlayer sliding^{43,44} induced out-of-plane ferroelectricity in bilayer WTe₂ has been verified experimentally^{16–19}. The -P state is the mirror image of +P state, as shown in Fig. 3a. Figure 3b shows the band structures of +P and -P states, where the valence and conduction bands overlap in our calculation.

The calculated in-plane BPVE coefficients are shown in Fig. 3c. There are three independent tensor elements σ_{xy}^x , σ_{xx}^y , σ_{yy}^y , and $\sigma_{xx}^x = \sigma_{yy}^y = \sigma_{xy}^y = 0$ due to the C_{1v} symmetry. The calculated in-plane BPVE coefficients are the same in two opposite ferroelectric orders: $\sigma_{xy}^x(+P) = \sigma_{xy}^x(-P)$, $\sigma_{xx}^y(+P) = \sigma_{xx}^y(-P)$, $\sigma_{yy}^y(+P) = \sigma_{yy}^y(-P)$, which is consistent with the above symmetry analysis. The in-plane BPVE photocurrent with the direction of polarization of light is shown in Fig. 3d, which shows \hat{M}_{yz} symmetry, and its magnitude is dependent on the light (see Supplementary Note 4 for details). Recently, it was shown that bilayer WTe₂ exhibits unswitchable in-plane nonlinear anomalous Hall effect^{14,18}.

On the contrary, the out-of-plane BPVE coefficients switch with the change of ferroelectric order, $\sigma_{xx}^z(+P) = -\sigma_{xx}^z(-P)$, $\sigma_{yy}^z(+P) = -\sigma_{yy}^z(-P)$ [Fig. 3e]. Unlike the bilayer MoS₂, the out-of-plane BPVE coefficients show anisotropy $\sigma_{xx}^z \neq \sigma_{yy}^z$ ($\sigma_{xy}^z = \sigma_{yx}^z = 0$) for each

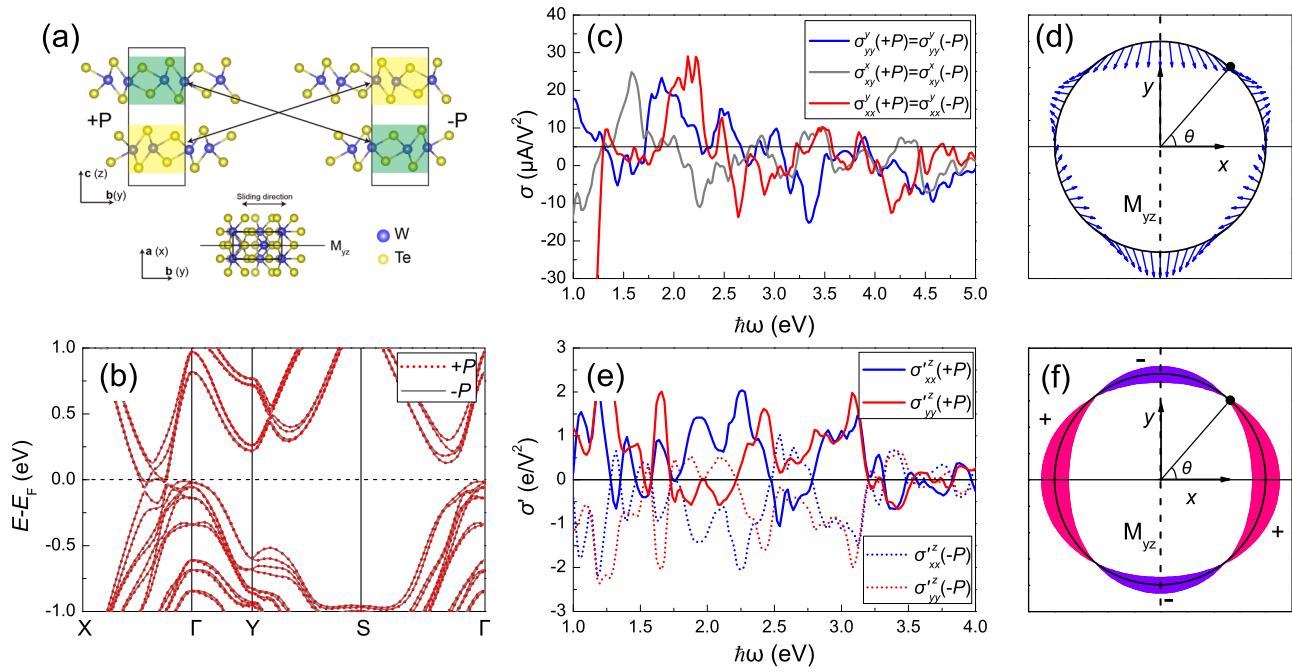


Fig. 3 Calculated results of ferroelectric bilayer WTe_2 . **a** Crystal structure. $+P$ and $-P$ states are adopted from ref. ⁴³. Rectangle in **a** represents the unit cell, and the double-arrrows line means the monolayer transformation under \hat{M}_{xy} symmetry. The lower panel in **a** denotes the top view of bilayer WTe_2 with $+P$ state. **b** Band structures of the $+P$ and $-P$ states. **c** In-plane and **e** out-of-plane BPVE coefficients. **d** In-plane BPVE photocurrent and **f** out-of-plane BPVE polarization of the $+P$ states with the different directions of polarization of light. The length of arrows in **d** indicates the magnitude of in-plane BPVE response (in arbitrary unit), where $\sigma_{xy}^x : \sigma_{xy}^y = 1 : 0.7 : -1.6$. The width and the color of the ribbon in **f** denote the magnitude and direction of out-of-plane BPVE response, and $\sigma_{xx}^z : \sigma_{yy}^z = 1 : -0.6$.

ferroelectric state due to the absence of in-plane C_3 symmetry, leading to the out-of-plane BPVE polarization is dependent on the polarization of light as shown in Fig. 3f. Recently, ZrI_2 , a sister material of polar semimetals WTe_2 , is also demonstrated^{45–47} to have interlayer-sliding ferroelectricity. Similar BPVE behaviors with bilayer WTe_2 are expected to be observed due to the same symmetry and interlayer-stacking way (Case 1b).

The calculated values of the in-plane BVPE coefficient of bilayer MoS_2 and bilayer WTe_2 are comparable to the reported monolayer MX [M = (Ge, Sn) and X = (Se, S)]^{13,48} and larger than 3D conventional ferroelectric materials (such as BiFeO_3 ⁴⁹, BiTiO_3 , and PbTiO_3 ²). The out-of-plane BPVE coefficients are comparable to twisted bilayers graphene³², which induces voltage are detectable experimentally. We can distinguish the photo-induced polarization and intrinsic polarization of interlayer-sliding ferroelectric materials in two subsequent detections with/without light in experiments.

We can calculate the light-induced out-of-plane electric dipole moment and voltage caused by the out-of-plane BPVE, and estimate the possibility to flip the ferroelectric order. With light power of $2.65 \times 10^{11} \text{ W/cm}^2$ (equivalent electric field $E=1 \text{ V/nm}$) and a typical value of $\sigma_{xx}^z = \sigma_{yy}^z = 1 \text{ e/V}^2$ for the out-of-plane BPVE coefficients, the light-induced polarization $p_z = 1 \text{ e/nm}^2$, meanwhile the light-induced voltage difference between the two layers ($V = p_z d / \epsilon_0$, $d = 1 \text{ nm}$) is found to be 1.8 V . The photo-induced polarization is already bigger than intrinsic polarization of interlayer-sliding ferroelectric materials (about 0.01 e/nm^2)¹⁵, and the photo-induced out-of-plane voltage is also bigger than the flipping voltage (about 0.1 V/nm) in experiments^{16–25}. Therefore, we think the photo-induced polarization can flip the ferroelectric order when the laser intensity is larger enough. Recently, experiment⁵⁰ shows that the stacking order in bulk WTe_2 can be manipulated by ultrafast optical excitation, which indicates the possibility for the flip the ferroelectric order by optical irradiation. The kinetic process of ferroelectric phase transition under light is

beyond the scope of current work, which needs to be further studied.

In our work, we only studied BPVE caused by the electronic shift current mechanism. While recently studies^{51–53} showed that excitons can enhance BPVE even above the band gap. The exciton effect on the BPVE in interlayer-sliding ferroelectric materials is deserved further study, however, the BPVE behavior with the ferroelectric order should not be changed because it is constrained by symmetry.

DISCUSSION

According to the above two specific examples, the in-plane BPVE is invariant, while the out-of-plane BPVE reverses with the change of ferroelectric order in interlayer-sliding ferroelectric materials. The ferroelectric order and BPVE in bilayer interlayer sliding ferroelectric materials are subject to different symmetry transformation rules, and do not always synchronize. The study of non-synchronous BPVE with the ferroelectric order in mirror symmetry-related ferroelectric materials allows the comprehension of the relationship between them in another view.

Moreover, these BPVE characters in 2D interlayer-sliding ferroelectric materials will lead to distinctive photovoltaic phenomena and applications in photoelectric devices. The in-plane BPVE photocurrents in a single crystal of interlayer-sliding ferroelectric materials are invariant with two opposite ferroelectric domains, thus the photovoltaic currents between different domains superimpose rather than cancel, as shown in Fig. 4. Since ferroelectric domains are often unavoidable in real materials, especially for the interlayer-sliding ferroelectric materials fabricated via the tear-and-stack method^{20,21,25,54}. Therefore, this unswitchable BPVE feature boosts the development of large-scale photoelectric devices that are immune to the polarization of ferroelectric domains. Nevertheless, the out-of-plane BPVE inverses between

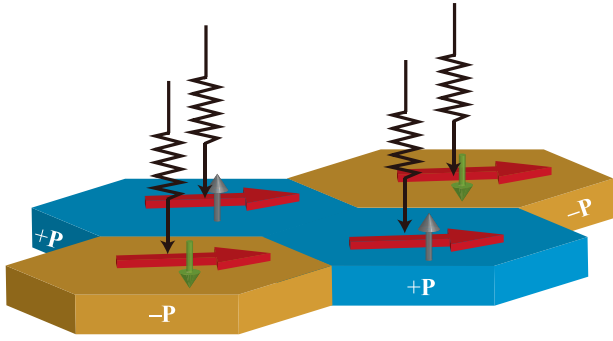


Fig. 4 In-plane and out-of-plane BPVE response with opposite ferroelectric domains for interlayer-sliding ferroelectric materials. The horizontal and vertical arrows denote the in-plane BPVE current and out-of-plane BPVE polarization, respectively.

the opposite ferroelectric orders (Fig. 4), which can be utilized to construct switchable photoelectric devices.

In conclusion, we use the abstract bilayer crystal model to analyze the symmetries of the four most common cases of bilayer vdW materials with interlayer sliding and found two cases (Case 1b and Case 2a) can have the possibility to achieve the interlayer-sliding ferroelectricity, which the interlayer-sliding ferroelectric materials found in experiments fall into. We revealed that the opposite ferroelectric states in the interlayer-sliding ferroelectric materials are linked by the horizontal mirror symmetry, leading to the in-plane BPVE being invariant while the out-of-plane BPVE switches with opposite ferroelectric states. BPVE in all directions of interlayer-sliding ferroelectric materials are not flipped synchronously with the ferroelectric orders, which is different from the scenario occurs in traditional ferroelectric materials. Our theoretical study provides a strategy for a comprehensive understanding of the relationship between the ferroelectric order and BPVE in 2D interlayer-sliding ferroelectric materials. Moreover, the switchable out-of-plane BPVE can be used to design switchable photoelectric devices. On the other hand, the in-plane BPVE is robust against the ferroelectric order, and the unswitchable character is beneficial to construct larger-scale photoelectric devices.

METHODS

In-plane and out-of-plane BPVE theory

According to the second-order Kubo formalism theory^{33,34}, σ_{bc}^a in the Eq. (1) of the main text can be expressed as

$$\sigma_{bc}^a \equiv \frac{1}{2} \text{Re} \{ \chi_{bc}^a + \chi_{cb}^a \}, \quad (5)$$

where

$$\chi_{bc}^a(\omega) = -\frac{e^3}{(\hbar\omega)^2} \int \frac{d\mathbf{k}}{(2\pi)^3} \sum_{mnl} \frac{f_{lm} v_{lm}^b}{E_{ml} - \hbar\omega + i\delta} \left(\frac{v_{mn}^a v_{nl}^c}{E_{mn} + i\delta} - \frac{v_{mn}^c v_{nl}^a}{E_{nl} + i\delta} \right), \quad (6)$$

$\delta = \hbar/\tau$, and τ is the lifetime, ω is the frequency of the light, f_{lm} and E_{ml} are the difference of occupation number and band energy between bands l and m .

Within a modified second-order Kubo formalism theory³², the out-of-plane BPVE coefficient in Eq. (2) of the main text can be expressed as

$$\sigma_{bc}^z \equiv \frac{1}{2} \text{Re} \{ \chi_{bc}^z + \chi_{cb}^z \}, \quad (7)$$

and

$$\chi_{bc}^z = \frac{e^2}{(\hbar\omega)^2} \int \frac{d\mathbf{k}}{(2\pi)^3} \sum_{mnl} \frac{f_{lm} v_{lm}^b}{E_{ml} - \hbar\omega + i\delta} \left(\frac{(p_z)_{nm} v_{nl}^c}{E_{mn} + i\delta} - \frac{v_{mn}^c (p_z)_{nl}}{E_{nl} + i\delta} \right), \quad (8)$$

where $(p_z)_{nm} = \langle n | \hat{p}_z | m \rangle$ is the out-of-plane dipole matrix element, and \hat{p}_z is the out-of-plane dipole operator. The interatomic electric dipoles due to the overlapping of wave functions should be very small, which was ignored in our calculation. \hat{p}_z contributed by interatomic electric dipole

only has nonzero diagonal components which can be expressed as

$$\hat{p}_z = -e \begin{bmatrix} r_{1,z} & 0 & \cdots \\ 0 & r_{2,z} & \cdots \\ \vdots & \vdots & \ddots \end{bmatrix} \quad (9)$$

where $r_{i,z}$ is the z -component position of the i -th atom. We define the middle of the 2D materials as the origin: $\sum r_{i,z} = 0$. Equation (6) is very similar to Eq. (8), except for the position operator $\hat{p}_{i,z}$ instead of the velocity operator.

First-principles calculations

The first-principles calculations based on density functional theory (DFT) are performed by using the VASP package. General gradient approximation (GGA) according to the Perdew–Burke–Ernzerhof (PBE) functional is used. The energy cutoff of the plane wave basis is set to 400 eV. The Brillouin zone is sampled with a $12 \times 12 \times 1$ ($12 \times 8 \times 1$) mesh of \mathbf{k} -points for MoS₂ (WTe₂). To simulate the monolayers, vacuum layers (~15 Å) are introduced. The vdW force with DFT-D2 correction is considered in the main text. The calculation results and corresponding discussions using vdW force with DFT-D3 correction are shown in Supplementary Note 6. Spin-orbital coupling effects are considered for bilayer MoS₂ and WTe₂ in the band structure and BPVE calculations.

The DFT Bloch wave functions are iteratively transformed into maximally localized Wannier functions by the Wannier90 code^{55,56}. Mo- d and S- p ($W-d$ and Te- p) orbitals are used to construct the Wannier functions for MoS₂ (WTe₂). The in-plane and out-of-plane BPVE coefficients are calculated by our own program WNLOP (Wannier Nonlinear Optics Package) based on effective tight-binding (TB) Hamiltonian. A convergence test of \mathbf{k} -mesh is performed, and $500 \times 500 \times 1$ ($600 \times 300 \times 1$) \mathbf{k} -mesh is sufficient in BPVE calculations of MoS₂ (WTe₂). We adopt $\delta = 0.02$ eV for Eq. (6) and Eq. (8) in our calculation to take into account various relaxation processes.

The 3D-like BPVE coefficients are obtained assuming an active single-layer with a thickness of L_{active} ¹³

$$\sigma_{3D} = \frac{L_{\text{slab}}}{L_{\text{active}}} \sigma_{\text{slab}}, \quad (10)$$

where σ_{slab} is the calculated BPVE coefficient, and L_{slab} ($L_{\text{active}} < L_{\text{slab}}$) is the effective thickness slab.

DATA AVAILABILITY

The authors declare that all source data supporting the findings of this study are available within the article and the Supplementary Information file.

CODE AVAILABILITY

The calculating codes are available from the corresponding authors upon reasonable request.

Received: 20 January 2022; Accepted: 2 June 2022;

Published online: 01 July 2022

REFERENCES

- Sipe, J. E. & Shkrebtii, A. I. Second-order optical response in semiconductors. *Phys. Rev. B* **61**, 5337–5352 (2000).
- Young, S. M. & Rappe, A. M. First principles calculation of the shift current photovoltaic effect in ferroelectrics. *Phys. Rev. Lett.* **109**, 116601 (2012).
- Tan, L. Z. et al. Shift current bulk photovoltaic effect in polar materials—hybrid and oxide perovskites and beyond. *npj Comput. Mater.* **2**, 16026 (2016).
- Paillard, C. et al. Photovoltaics with ferroelectrics: current status and beyond. *Adv. Mater.* **28**, 5153–5168 (2016).
- Pandey, R. et al. Mutual insight on ferroelectrics and hybrid halide perovskites: a platform for future multifunctional energy conversion. *Adv. Mater.* **31**, e1807376 (2019).
- Choi, T., Lee, S., Choi, Y. J., Kiryukhin, V. & Cheong, S.-W. Switchable ferroelectric diode and photovoltaic effect in BiFeO₃. *Science* **324**, 63–66 (2009).
- Ji, W., Yao, K. & Liang, Y. C. Bulk photovoltaic effect at visible wavelength in epitaxial ferroelectric BiFeO₃ thin films. *Adv. Mater.* **22**, 1763–1766 (2010).

8. Grinberg, I. et al. Perovskite oxides for visible-light-absorbing ferroelectric and photovoltaic materials. *Nature* **503**, 509–512 (2013).
9. Lee, D. et al. Polarity control of carrier injection at ferroelectric/metal interfaces for electrically switchable diode and photovoltaic effects. *Phys. Rev. B* **84**, 125305 (2011).
10. Li, Y. et al. Enhanced bulk photovoltaic effect in two-dimensional ferroelectric CuInP_2S_6 . *Nat. Commun.* **12**, 5896 (2021).
11. Nakamura, M. et al. Shift current photovoltaic effect in a ferroelectric charge-transfer complex. *Nat. Commun.* **8**, 281 (2017).
12. Kim, J. et al. Prediction of ferroelectricity-driven Berry curvature enabling charge- and spin-controllable photocurrent in tin telluride monolayers. *Nat. Commun.* **10**, 3965 (2019).
13. Wang, H. & Qian, X. Ferroicity-driven nonlinear photocurrent switching in time-reversal invariant ferroic materials. *Sci. Adv.* **5**, eaav9743 (2019).
14. Wang, H. & Qian, X. Ferroelectric nonlinear anomalous Hall effect in few-layer WTe_2 . *npj Comput. Mater.* **5**, 119 (2019).
15. Li, L. & Wu, M. Binary compound bilayer and multilayer with vertical polarizations: two-dimensional ferroelectrics, multiferroics, and nanogenerators. *ACS Nano* **11**, 6382–6388 (2017).
16. Fei, Z. et al. Ferroelectric switching of a two-dimensional metal. *Nature* **560**, 336–339 (2018).
17. Sharma, P. et al. A room-temperature ferroelectric semimetal. *Sci. Adv.* **5**, eaax5080 (2019).
18. Xiao, J. et al. Berry curvature memory through electrically driven stacking transitions. *Nat. Phys.* **16**, 1028–1034 (2020).
19. de la Barrera, S. C. et al. Direct measurement of ferroelectric polarization in a tunable semimetal. *Nat. Commun.* **12**, 5298 (2021).
20. Yasuda, K., Wang, X., Watanabe, K., Taniguchi, T. & Jarillo-Herrero, P. Stacking-engineered ferroelectricity in bilayer boron nitride. *Science* **372**, 1458–1462 (2021).
21. Stern, M. V. et al. Interfacial ferroelectricity by van der Waals sliding. *Science* **372**, 1462–1466 (2021).
22. Hu, H. et al. Room-temperature out-of-plane and in-plane ferroelectricity of two-dimensional β -InSe nanoflakes. *Appl. Phys. Lett.* **114**, 252903 (2019).
23. Hu, H. et al. Out-of-plane and in-plane ferroelectricity of atom-thick two-dimensional InSe. *Nanotechnology* **32**, 385202 (2021).
24. Wang, X. et al. Interfacial ferroelectricity in rhombohedral-stacked bilayer transition metal dichalcogenides. *Nat. Nanotechnol.* **17**, 367–371 (2022).
25. Weston, A. et al. Interfacial ferroelectricity in marginally twisted 2D semiconductors. *Nat. Nanotechnol.* **17**, 390–395 (2022).
26. Wu, M. & Jena, P. The rise of two-dimensional van der Waals ferroelectrics. *Wires Comput. Mol. Sci.* **8**, e1365 (2018).
27. Cui, C., Xue, F., Hu, W.-J. & Li, L.-J. Two-dimensional materials with piezoelectric and ferroelectric functionalities. *npj 2D Mater. Appl.* **2**, 18 (2018).
28. Guan, Z. et al. Recent progress in two-dimensional ferroelectric. *Mater. Adv. Electron. Matter* **6**, 1900818 (2020).
29. Qi, L., Ruan, S. & Zeng, Y. J. Review on recent developments in 2D ferroelectrics: theories and applications. *Adv. Mater.* **33**, 2005098 (2021).
30. Mounet, N. et al. Two-dimensional materials from high-throughput computational exfoliation of experimentally known compounds. *Nat. Nanotechnol.* **13**, 246–252 (2018).
31. Hastrup, S. et al. The computational 2D materials database: high-throughput modeling and discovery of atomically thin crystals. *2D Matter* **5**, 042002 (2018).
32. Gao, Y., Zhang, Y. & Xiao, D. Tunable layer circular photogalvanic effect in twisted bilayers. *Phys. Rev. Lett.* **124**, 077401 (2020).
33. Kraut, W. & von Baltz, R. Anomalous bulk photovoltaic effect in ferroelectrics: a quadratic response theory. *Phys. Rev. B* **19**, 1548–1554 (1979).
34. von Baltz, R. & Kraut, W. Theory of the bulk photovoltaic effect in pure crystals. *Phys. Rev. B* **23**, 5590–5596 (1981).
35. Lihm, J.-M. & Park, C.-H. Wannier function perturbation theory: localized representation and interpolation of wave function perturbation. *Phys. Rev. X* **11**, 041053 (2021).
36. Ibañez-Azpiroz, J., Tsirkin, S. S. & Souza, I. Ab initio calculation of the shift photocurrent by Wannier interpolation. *Phys. Rev. B* **97**, 245143 (2018).
37. Pizzi, G. et al. Wannier90 as a community code: new features and applications. *J. Phys.: Condens. Matter* **32**, 165902 (2019).
38. Ahn, J., Guo, G.-Y., Nagaosa, N. & Vishwanath, A. Riemannian geometry of resonant optical responses. *Nat. Phys.* **18**, 290–295 (2022).
39. Ahn, J., Guo, G.-Y. & Nagaosa, N. Low-frequency divergence and quantum geometry of the bulk photovoltaic effect in topological semimetals. *Phys. Rev. X* **10**, 041041 (2020).
40. Xiao, R.-C., Shao, D.-F., Huang, W. & Jiang, H. Electrical detection of ferroelectriclike metals through the nonlinear Hall effect. *Phys. Rev. B* **102**, 024109 (2020).
41. Zhang, Y. et al. Switchable magnetic bulk photovoltaic effect in the two-dimensional magnet CrI_3 . *Nat. Commun.* **10**, 3783 (2019).
42. Xiao, R.-C., Shao, D.-F., Li, Y.-H. & Jiang, H. Spin photogalvanic effect in two-dimensional collinear antiferromagnets. *npj Quant. Mater.* **6**, 35 (2021).
43. Yang, Q., Wu, M. & Li, J. Origin of two-dimensional vertical ferroelectricity in WTe_2 bilayer and multilayer. *J. Phys. Chem. Lett.* **9**, 7160–7164 (2018).
44. Liu, X. et al. Vertical ferroelectric switching by in-plane sliding of two-dimensional bilayer WTe_2 . *Nanoscale* **11**, 18575–18581 (2019).
45. Zhang, T. et al. Ferroelastic-ferroelectric multiferroics in a bilayer lattice. *Phys. Rev. B* **103**, 165420 (2021).
46. Ding, N. et al. Phase competition and negative piezoelectricity in interlayer-sliding ferroelectric ZrI_2 . *Phys. Rev. Mater.* **5**, 084405 (2021).
47. Ma, X., Liu, C., Ren, W. & Nikolaev, S. A. Tunable vertical ferroelectricity and domain walls by interlayer sliding in β - ZrI_2 . *npj Comput. Mater.* **7**, 177 (2021).
48. Rangel, T. et al. Large bulk photovoltaic effect and spontaneous polarization of single-layer monochalcogenides. *Phys. Rev. Lett.* **119**, 067402 (2017).
49. Young, S. M., Zheng, F. & Rappe, A. M. First-principles calculation of the bulk photovoltaic effect in bismuth ferrite. *Phys. Rev. Lett.* **109**, 236601 (2012).
50. Ji, S., Grånäs, O. & Weissenrieder, J. Manipulation of stacking order in Td-WTe_2 by ultrafast optical excitation. *ACS Nano* **15**, 8826–8835 (2021).
51. Chan, Y.-H., Qiu, D. Y., Jornada, F. H. D. & Louie, S. G. Giant exciton-enhanced shift currents and direct current conduction with subbandgap photo excitations produced by many-electron interactions. *P. Natl Acad. Sci. USA* **118**, e1906938118 (2021).
52. Konabe, S. Exciton effect on shift current in single-walled boron-nitride nanotubes. *Phys. Rev. B* **103**, 075402 (2021).
53. Fei, R., Tan, L. Z. & Rappe, A. M. Shift-current bulk photovoltaic effect influenced by quasiparticle and exciton. *Phys. Rev. B* **101**, 045104 (2020).
54. Zheng, Z. et al. Unconventional ferroelectricity in moire heterostructures. *Nature* **588**, 71–76 (2020).
55. Mostofi, A. A. et al. wannier90: a tool for obtaining maximally-localised Wannier functions. *Comput. Phys. Commun.* **178**, 685–699 (2008).
56. Mostofi, A. A. et al. An updated version of wannier90: a tool for obtaining maximally-localised Wannier functions. *Comput. Phys. Commun.* **185**, 2309–2310 (2014).
57. Jain, A. et al. Commentary: the materials project: a materials genome approach to accelerating materials innovation. *APL Mater.* **1**, 011002 (2013).

ACKNOWLEDGEMENTS

The authors acknowledge the High-performance Computing Platform of Anhui University for providing computing resources. We thank Bin Xu, Ding-Fu Shao, Yuan-Jun Jin, and Xue Liu for their useful discussions. This work is supported by the National Natural Science Foundation of China under No. 11947212, Natural Science Foundation of Anhui Province under No. 110158162022, in part by the Joint Funds of the National Natural Science Foundation of China and the Chinese Academy of Sciences Large-Scale Scientific Facility under Grant No. U1932156, and in part by the Natural Science Foundation of Anhui Province under Grant No. 2008085QA29. Y.G. and R.-C.X. acknowledge the startup foundation from USTC and AHU, respectively.

AUTHOR CONTRIBUTIONS

R.-C.X. conceived the project with H.L. and edited the code and performed the first-principles calculations. R.-C.X. performed the symmetry analysis and Y.G. checked it. R.-C.X., Y.G., and H.L. discussed the results and the writing. The manuscript was written through the contributions of all authors. All authors have approved the final version of the manuscript.

COMPETING INTERESTS

The authors declare no competing interests.

ADDITIONAL INFORMATION

Supplementary information The online version contains supplementary material available at <https://doi.org/10.1038/s41524-022-00828-1>.

Correspondence and requests for materials should be addressed to Yang Gao or Hui Li.

Reprints and permission information is available at <http://www.nature.com/reprints>

Publisher's note Springer Nature remains neutral with regard to jurisdictional claims in published maps and institutional affiliations.



Open Access This article is licensed under a Creative Commons Attribution 4.0 International License, which permits use, sharing, adaptation, distribution and reproduction in any medium or format, as long as you give appropriate credit to the original author(s) and the source, provide a link to the Creative Commons license, and indicate if changes were made. The images or other third party material in this article are included in the article's Creative Commons license, unless indicated otherwise in a credit line to the material. If material is not included in the article's Creative Commons license and your intended use is not permitted by statutory regulation or exceeds the permitted use, you will need to obtain permission directly from the copyright holder. To view a copy of this license, visit <http://creativecommons.org/licenses/by/4.0/>.

© The Author(s) 2022